(Read at Autumn Meeting of the Society of Naval Architects of Japan, Nov. 1990)

A Cell-Centered, Finite-Volume Upwind Scheme with Global Conservation

by Yoshiaki Kodama*, *Member*

Summary

A finite-volume, conservative upwind scheme has been developed, based on the flux-difference splitting method. Pseudo-compressibility is introduced to the continuity equation. The cell-centered is adopted, i. e., nodes for flow variables were placed at the center of each grid cell. With this combination of the scheme and the node-cell layout, the global conservation property has been derived in a straightforward manner.

The scheme was applied to two types of flows. First the flow past a circular cylinder was computed using the O-grid at the Reynolds number $R_e=40$. The integrated momentum and mass fluxes at inner and outer boundaries agreed up to more than 9 significant figures after 1,000 time steps. Thus the global conservation property was confirmed. The computed drag coefficient value agreed well with other computed values. The same flow was computed using the H-grid. The drag coefficient value thus obtained differed very little from the O-grid value.

The flow past a flat plate with a point of mapping singularity was computed at an attack angle of 30 degrees. It was confirmed that the global conservation property of the present scheme is not affected by the presence of mapping singularities.

1. Introduction

Researchers in CFD (Computational Fluid Dynamics) make efforts such that their computer codes mimic the real physical fluid phenomena as accurately as possible. CFD starts with the discretization of the governing equations of fluid motions, i. e. the conservation laws of mass, momentum, and so on. However, the discretization inevitably causes some amount of loss of information in the original equations. Since the most important information to be retained is the conservation property, one naturally chooses to use conservative schemes.

Accurate estimation of the drag of a ship progressing steadily in calm water is important for ship's powering and performance predictions. Though the flow has been computed by many researchers including the present author[1],[2],[3],[4],[5],[6], it remains as quite a challenging task for CFD, because drag of a streamlined body is difficult to compute accurately compared with lift. A flaw in a computational scheme, which is negligible for lift, can cause significant harm on drag.

This paper deals whth an effort to give a sound basis toward accurate computation of the drag of a ship, by removing the "flaws" in computational schemes. Global conservation is pursued here. The word "global conservation" means that the conservation property is satisfied everywhere in the computed flow domain, all the way down to boundaries. If it is satisfied, the drag computed by the wake survey method agrees with that obtained by integration on the body surface, for example.

This paper presents a scheme possessing global conservation property. The discretized governing equations are made fully consistent with the way the momentum fluxes are integrated to compute lift and drag. An upwind flux-difference-splitting method in the finite volume framework is used for discretization. Pseudo-compressibility is introduced in the continuity equation, in order to couple the equation with those for the momentum. Global mass conservation is satisfied in the steady-state limit. Nodes for flow variables are placed at the center of each grid cell. This allows the use of grid cells as control volumes, from which global conservation property is automatically derived, even when points of mapping singularity are present in the domain.

2. Formulation

2.1 Cell-centered method

This section shows how the "flaws" that exist in conventional methods and prevent global conservation can be removed by adopting the cell-centered method.

Fig. 1(a) shows layouts of control volumes in the present node approach and the conventional node approach. Conventionally, in the pseudo-compressibility

* Ship Research Institute

method adopted by the author[6], the nodes for flow variables are placed at the grid nodes. There the control volume used for conservation laws is bordered by edges located at half-way points between the nodes. As its consequence the half grid-cell area adjacent to boundaries (solid wall, e. g.) cannot be covered in a straightforward manner. Global conservation is violated there. In the cell-centered method[7], flow variable nodes are placed at the center of each grid cell, which is used as a control volume. This time the gap does not occur, and global conservation holds in a straightforward manner.

Fig. 1(b) shows the situation at a junction, which typically occurs with grids of H topology. If the flow comes from left with non-zero at tack angle as shown in the figure, a large pressure difference occurs near the leading edge between upperside and lowerside. With the conventional node layout, the pressure value is required at the junction point. A multi-valuedness problem of the pressure there occurs, since, if it is extrapolated from lowerside, high pressure will result, and if extrapolated from upperside, low pressure will result. Simply taking an average often causes pressure oscillation. It should be noted that the drag of a streamlined body can be significantly influenced by the pressure values at leading and trailing edge points. In the cell-centered node approach, in contrast, the multi-valuedness problem does not occur, because no flow variable node is defined multiply. Global conservation is automatically satisfied there, too.

Fig. 1(c) shows the situation with a point of mapping singularity, which exists in a grid of H-O topology around a ship hull. The transformed governing equations become singular at the point, and cannot be computed. In the conventional node approach, the flow values there are usually obtained by interpolation using neighboring points, and global conservation is violated. In the cell-centered method, the point of mapping singularity is automatically circumvented, and global conservation holds.

2.2 Governing equations

The nondimensional governing equations[6], i. e. the conservation of momentum and mass are written in Cartesian coordinates as

$$\frac{\partial q}{\partial t}+\frac{\partial F}{\partial x}+\frac{\partial G}{\partial y}+\frac{\partial F_v}{\partial x}+\frac{\partial G_v}{\partial y}=0 \qquad (1)$$

where

$$q=\begin{bmatrix}u\\v\\p\end{bmatrix},\quad F=\begin{bmatrix}u^2+p\\uv\\\beta u\end{bmatrix},\quad G=\begin{bmatrix}uv\\v^2+p\\\beta v\end{bmatrix}$$

$$F_v=-\frac{1}{R_e}\begin{bmatrix}2u_x\\u_y+v_x\\0\end{bmatrix},\quad G_v=-\frac{1}{R_e}\begin{bmatrix}u_y+v_x\\2v_y\\0\end{bmatrix}$$

where all the subscripts x and y denote partial derivatives. β is a positive constant for the added pseudo-compressibility. Coordinate transformations from (x, y) to (ξ, η) coordinates are then made. Thus

$$S\frac{\partial q}{\partial t}+\frac{\partial \hat{F}}{\partial \xi}+\frac{\partial \hat{G}}{\partial \eta}+\frac{\partial \hat{F}_v}{\partial \xi}+\frac{\partial \hat{G}_v}{\partial \eta}=0 \qquad (2)$$

where

$$\begin{cases}\hat{F}=(kn_x)^{\xi}F+(kn_y)^{\xi}G\\ \hat{G}=(kn_x)^{\eta}F+(kn_y)^{\eta}G\end{cases},$$

and similarly with $\hat{F}_v$ and $\hat{G}_v$.

$$\begin{cases}k^{\xi}=\sqrt{x_\eta^2+y_\eta^2},\ (kn_x)^{\xi}=y_\eta,\ (kn_y)^{\xi}=-x_\eta\\ k^{\eta}=\sqrt{x_\xi^2+y_\xi^2},\ (kn_x)^{\eta}=-y_\xi,\ (kn_y)^{\eta}=x_\xi\end{cases}$$

where S is the local area or Jacobian. The corresponding semi-discrete form is, by using (i, j) as indices in (ξ, η) directions,

$$S_{i,j}\frac{\partial q}{\partial t}+\hat{F}_{i+\frac{1}{2}}-\hat{F}_{i-\frac{1}{2}}+\hat{G}_{j+\frac{1}{2}}-\hat{G}_{j-\frac{1}{2}}+\hat{F}_{v_{i+1/2}}-\hat{F}_{v_{i-1/2}}+\hat{G}_{v_{j+1/2}}-\hat{G}_{v_{j-1/2}}=0. \qquad (3)$$

2.3 Inviscid terms

The flux-difference splitting method[1],[8],[9],[10],[11],[12] is used to construct the inviscid terms. The method is

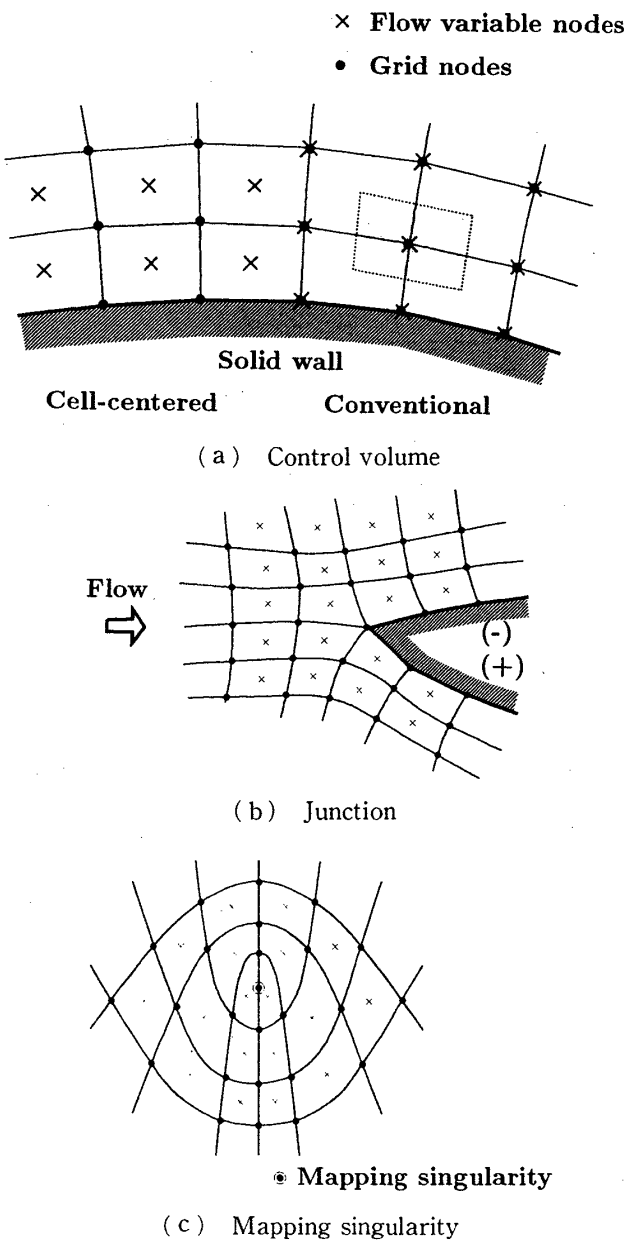

Fig. 1 Node layout in the cell-centered method.

widely used in TVD schemes for conservative, non-oscillatory shock-capturing purposes in compressible flow computations.

As a building block to form representations for the flux values in eq.(3), a flux difference between adjacent points is first defined. Using the Roe's averaging[12], the flux difference between the points at (i) and $(i+1)$ is defined as (Fig. 2)

$$\delta\hat{F}_{i+\frac{1}{2}}\equiv\hat{F}(q_{i+1},N_{i+\frac{1}{2}})-\hat{F}(q_i,N_{i+\frac{1}{2}})=A_{i+\frac{1}{2}}\delta q_{i+\frac{1}{2}}, \tag{4}$$

where N stands for the metrics, i.e., k, n_x, and n_y. A is the Jacobian matrix such as

$$A=\begin{bmatrix} 2kn_xu+kn_yv, & kn_yu, & kn_x \\ kn_xv, & kn_xu+2kn_yv, & kn_y \\ kn_x\beta, & kn_y\beta, & 0 \end{bmatrix} \tag{5}$$

where

$$\begin{cases} u=(u_i+u_{i+1})/2 \\ v=(v_i+v_{i+1})/2 \\ k=k^{\xi},\ n_x=n_x^{\xi},\ n_y=n_y^{\xi} \end{cases}$$

and $\delta q_{i+\frac{1}{2}}$ is defined as

$$\delta q_{i+\frac{1}{2}}=q_{i+1}-q_i. \tag{6}$$

All the metrics in eq.(4) are evaluated at $i+1/2$. This makes possible the Jacobian representation shown in the rightmost equality of the same equation.

The next thing to do is to split the flux difference into positive and negative parts by splitting the Jacobian matrix A into positive and negative parts depending on the signs of the eigenvalues. That is,

$$\delta\hat{F}_{i+\frac{1}{2}}=\delta\hat{F}^{+}_{i+\frac{1}{2}}+\delta\hat{F}^{-}_{i+\frac{1}{2}} \tag{7}$$

$$\delta\hat{F}^{\pm}_{i+\frac{1}{2}}=(R\Lambda^{\pm}L)\delta q_{i+\frac{1}{2}}=A^{\pm}\delta q_{i+\frac{1}{2}} \tag{8}$$

where

$$R=[r_1,\ r_2,\ r_3]=\begin{bmatrix} u-(U+c)n_x, & -2n_y, & u-(U-c)n_x \\ v-(U+c)n_y, & 2n_x, & v-(U-c)n_y \\ c(U+c), & 0, & -c(U-c) \end{bmatrix} \tag{9}$$

$$L=\begin{bmatrix} l_1^T \\ l_2^T \\ l_3^T \end{bmatrix}=\frac{1}{2c^2}\begin{bmatrix} (U-c)n_x, & (U-c)n_y, & 1 \\ -(Uv+\beta n_y), & Uu+\beta n_x, & un_y-vn_x \\ (U+c)n_x, & (U+c)n_y, & 1 \end{bmatrix} \tag{10}$$

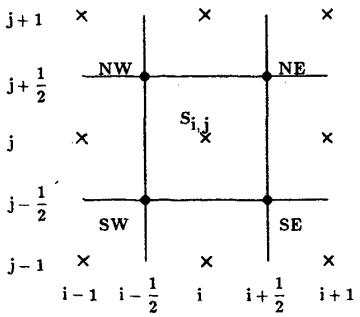

Fig. 2 Control volume.

$$\Lambda^{\pm}=\begin{bmatrix} \lambda_1^{\pm} & 0 & 0 \\ 0 & \lambda_2^{\pm} & 0 \\ 0 & 0 & \lambda_3^{\pm} \end{bmatrix} \quad \text{where} \quad \lambda_m^{\pm}=\frac{\lambda_m\pm|\lambda_m|}{2}$$

$$\begin{cases} \lambda_1=k(U-c),\ \lambda_2=kU,\ \lambda_3=k(U+c) \\ U=un_x+vn_y \\ c=\sqrt{U^2+\beta} \end{cases} \tag{11}$$

where "c" is the speed of sound in this pseudo-compressible world.

The metric terms are defined using the finite-volume approach as shown in Fig. 2. S_{ij}, the area of the cell (i, j), and metrics are defined as

$$S_{ij}=\frac{1}{2}|(x_{SW}-x_{NE})(y_{SE}-y_{NW})-(y_{SW}-y_{NE})(x_{SE}-x_{NW})| \tag{12}$$

$$\begin{cases} x_{\eta_{i+1/2}}=x_{NE}-x_{SE} \\ x_{\eta_{i-1/2}}=x_{NW}-x_{SW} \end{cases} \quad \begin{cases} x_{\xi_{i+1/2}}=x_{NE}-x_{NW} \\ x_{\xi_{i-1/2}}=x_{SE}-x_{SW}. \end{cases} \tag{13}$$

Using the flux difference in eq.(7), the flux values of up to 3rd-order accuracy are constructed with upwind differencing. The approach used here is the post-processing type (non-MUSCL type)[8],[9]. They are

$$\begin{aligned} \hat{F}_{i+\frac{1}{2}}&=\hat{F}_i(N_{i+\frac{1}{2}})+\Phi_1\delta\hat{F}^{+}_{i-\frac{1}{2}}+\Phi_2\delta\hat{F}^{+}_{i+\frac{1}{2}} \\ &\quad+(1-\Phi_2)\delta\hat{F}^{-}_{i+\frac{1}{2}}-\Phi_1\delta\hat{F}^{-}_{i+\frac{3}{2}} \\ \hat{F}_{i-\frac{1}{2}}&=\hat{F}_i(N_{i-\frac{1}{2}})+\Phi_1\delta\hat{F}^{+}_{i-\frac{3}{2}}+(\Phi_2-1)\delta\hat{F}^{+}_{i-\frac{1}{2}} \\ &\quad-\Phi_2\delta\hat{F}^{-}_{i-\frac{1}{2}}-\Phi_1\delta\hat{F}^{-}_{i+\frac{1}{2}} \end{aligned} \tag{14}$$

where the values of Φ_1 and Φ_2 are defined as

	1st-order upwind	Central	2nd up.	3rd up.
Φ_1	0	0	1/2	1/6
Φ_2	0	1/2	0	1/3

and the suffix (i) in $\hat{F}$ means that q is given at (i). Therefore

$$\begin{aligned} \hat{F}_{i+\frac{1}{2}}-\hat{F}_{i-\frac{1}{2}}&=\hat{F}_i(N_{i+\frac{1}{2}})-\hat{F}_i(N_{i-\frac{1}{2}}) \\ &\quad+\Gamma^{+}_{-\frac{3}{2}}\delta\hat{F}^{+}_{i-\frac{3}{2}}+\Gamma^{+}_{-\frac{1}{2}}\delta\hat{F}^{+}_{i-\frac{1}{2}} \\ &\quad+\Gamma^{+}_{\frac{1}{2}}\delta\hat{F}^{+}_{i+\frac{1}{2}}+\Gamma^{-}_{-\frac{1}{2}}\delta\hat{F}^{-}_{i-\frac{1}{2}} \\ &\quad+\Gamma^{-}_{\frac{1}{2}}\delta\hat{F}^{-}_{i+\frac{1}{2}}+\Gamma^{-}_{\frac{3}{2}}\delta\hat{F}^{-}_{i+\frac{3}{2}} \end{aligned} \tag{14.a}$$

where

$\Gamma^{+}_{-\frac{3}{2}}$	$\Gamma^{+}_{-\frac{1}{2}}$	$\Gamma^{+}_{\frac{1}{2}}$	$\Gamma^{-}_{-\frac{1}{2}}$	$\Gamma^{-}_{\frac{1}{2}}$	$\Gamma^{-}_{\frac{3}{2}}$
$-\Phi_1$	$1+\Phi_1-\Phi_2$	Φ_2	Φ_2	$1+\Phi_1-\Phi_2$	$-\Phi_1$

Note that the order of accuracy shown in the above equations is that in the computational space, and the accuracy in the physical space depends on the grid quality.

The eq.(14) is conservative in the sense that, by deriving another form for $\hat{F}_{i+1/2}$ by substituting $i+1$ into i in the second equation and equating that with the first, the eqs.(4) and (7) are derived. In other words, the eqs.(4) and (7) are sufficient to make the flux forms of eq.(14) conservative. If TVD flux limiters are applied to the flux differences in eq.(14), TVD schemes can be constructed. However, since no shock waves occur in the pseudocompressible world, and following the suggestion in ref. [11], TVD limiters have not been applied. Similar flux forms can be derived for $\hat{G}$.

The first two terms in the RHS of eq.(14.a) can be regarded as flux-correction terms that compensate for the flux imbalance caused by adopting the same index for the metrics in eq. (4). Fortunately, if the metrics are defined in a finite-volume manner as in eq. (13), these terms exactly cancel out with the corresponding terms in the j-direction when they are summed up to form the governing equation. That is

$$\hat{F}_{i,j}(N_{i+\frac{1}{2}})-\hat{F}_{i,j}(N_{i-\frac{1}{2}})+\hat{G}_{i,j}(N_{j+\frac{1}{2}})-\hat{G}_{i,j}(N_{j-\frac{1}{2}})=0. \tag{15}$$

The flux form in the i-($\xi-$) direction finally becomes

$$\hat{F}_{i+\frac{1}{2}}-\hat{F}_{i-\frac{1}{2}}=\sum_{m=-2}^{2}\tilde{M}_m q_{i+m} \tag{16}$$

where

$$\begin{cases}\tilde{M}_{-2}=-\Gamma^{+3}_{-\frac{3}{2}}A^{+}_{i-\frac{3}{2}}\\ \tilde{M}_{-1}=\Gamma^{+3}_{-\frac{3}{2}}A^{+}_{i-\frac{3}{2}}-(\Gamma^{+1}_{-\frac{1}{2}}A^{+}+\Gamma^{-1}_{-\frac{1}{2}}A^{-})_{i-\frac{1}{2}}\\ \tilde{M}_{0}=(\Gamma^{+1}_{-\frac{1}{2}}A^{+}+\Gamma^{-1}_{-\frac{1}{2}}A^{-})_{i-\frac{1}{2}}-(\Gamma^{+}_{\frac{1}{2}}A^{+}+\Gamma^{-}_{\frac{1}{2}}A^{-})_{i+\frac{1}{2}}\\ \tilde{M}_{1}=(\Gamma^{+}_{\frac{1}{2}}A^{+}+\Gamma^{-}_{\frac{1}{2}}A^{-})_{i+\frac{1}{2}}-\Gamma^{-3}_{\frac{3}{2}}A^{-}_{i+\frac{3}{2}}\\ \tilde{M}_{2}=\Gamma^{-3}_{\frac{3}{2}}A^{-}_{i+\frac{3}{2}}\end{cases} \tag{16.a}$$

Similarly in the j-($\eta-$) direction

$$\hat{G}_{j+\frac{1}{2}}-\hat{G}_{j-\frac{1}{2}}=\sum_{m=-2}^{2}\tilde{N}_m q_{j+m}. \tag{17}$$

2.4 Viscous terms

The viscous terms are derived in the same way as in ref.[9]. It is as follows. As shown in eq. (2) the viscous flux at $i+\frac{1}{2}$ is given as

$$\hat{F}_{v_{i+1/2}}=[(kn_x)^{\epsilon}F_v+(kn_y)^{\epsilon}G_v]_{i+\frac{1}{2}}$$

where

$$F_{v_{i+1/2}}=-\frac{1}{Re}\begin{bmatrix}2u_x\\ u_y+v_x\\ 0\end{bmatrix}_{i+\frac{1}{2}},\quad G_{v_{i+1/2}}=-\frac{1}{Re}\begin{bmatrix}u_y+v_x\\ 2v_y\\ 0\end{bmatrix}_{i+\frac{1}{2}}$$

The x- and y-derivatives of u in the above equation are computed by applying the Gauss integral theorem shown below

$$\iint u_x dxdy=\oint u dy,\quad \iint u_y dxdy=-\oint u dx \tag{18}$$

to the shaded area in Fig. 3. That is

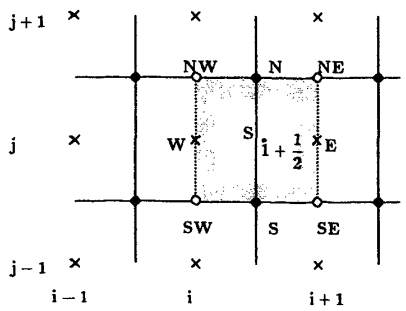

Fig. 3 Volume used for viscous term integration.

$$\begin{aligned}u_{x_{i+1/2}}&=\frac{1}{S_{i+\frac{1}{2}}}[u_E\delta y_E-u_N\delta y_N-u_W\delta y_W+u_S\delta y_S]\\ u_{y_{i+1/2}}&=-\frac{1}{S_{i+\frac{1}{2}}}[u_E\delta x_E-u_N\delta x_N-u_W\delta x_W+u_S\delta x_S]\end{aligned} \tag{19}$$

where

$$\delta y_E=y_{NE}-y_{SE},\quad \delta y_N=y_{NE}-y_{NW},\quad \text{etc.}$$

$$\begin{cases}u_E=u_{i+1,j}\\ u_N=\frac{1}{4}(u_{i+1,j+1}+u_{i+1,j}+u_{i,j+1}+u_{i,j})\\ u_W=u_{i,j}\\ u_S=\frac{1}{4}(u_{i+1,j}+u_{i+1,j-1}+u_{i,j}+u_{i,j-1})\end{cases}$$

and the area $S_{i+1/2}$ is computed using eq.(12). By explicitly picking out terms corresponding to q_i and q_{i+1} in order to prepare for IAF procedures, $F_{v_{i+\frac{1}{2}}}$ is given as

$$F_{v_{i+1/2}}=\left(\frac{\partial F_v}{\partial q_+}\right)_{i+\frac{1}{2}}q_{i+1}+\left(\frac{\partial F_v}{\partial q_-}\right)_{i+\frac{1}{2}}q_i+\bar{F}_{v_{i+1/2}} \tag{20}$$

where

$$\left(\frac{\partial F_v}{\partial q_\pm}\right)_{i+\frac{1}{2}}=-\frac{1}{Re}\begin{bmatrix}2\frac{\partial f_x}{\partial f_\pm} & 0 & 0\\ \frac{\partial f_y}{\partial f_\pm} & \frac{\partial f_x}{\partial f_\pm} & 0\\ 0 & 0 & 0\end{bmatrix}_{i-\frac{1}{2}}$$

$$\begin{cases}\left(\frac{\partial f_x}{\partial f_+}\right)_{i+\frac{1}{2}}=\frac{1}{S_{i+\frac{1}{2}}}\left[\delta y_E-\frac{1}{4}\delta y_N+\frac{1}{4}\delta y_S\right]\\ \left(\frac{\partial f_y}{\partial f_+}\right)_{i+\frac{1}{2}}=-\frac{1}{S_{i+\frac{1}{2}}}\left[\delta x_E-\frac{1}{4}\delta x_N+\frac{1}{4}\delta x_S\right]\end{cases}$$

$$\begin{cases}\left(\frac{\partial f_x}{\partial f_-}\right)_{i+\frac{1}{2}}=\frac{1}{S_{i+\frac{1}{2}}}\left[-\delta y_W-\frac{1}{4}\delta y_N+\frac{1}{4}\delta y_S\right]\\ \left(\frac{\partial f_y}{\partial f_-}\right)_{i+\frac{1}{2}}=-\frac{1}{S_{i+\frac{1}{2}}}\left[-\delta x_W-\frac{1}{4}\delta x_N+\frac{1}{4}\delta x_S\right]\end{cases}$$

$\bar{F}_{v_{i+1/2}}$ contains cross-derivative components. $G_{v_{i+1/2}}$ is given similarly as

$$G_{v_{i+1/2}}=\left(\frac{\partial G_v}{\partial q_+}\right)_{i+\frac{1}{2}}q_{i+1}+\left(\frac{\partial G_v}{\partial q_-}\right)_{i+\frac{1}{2}}q_i+\bar{G}_{v_{i+\frac{1}{2}}} \tag{21}$$

The form of the viscous flux at $i-\frac{1}{2}$ is obtained by substituting $i-1$ into i in the flux form at $i+\frac{1}{2}$. The viscous flux in the η-direction at $j+\frac{1}{2}$ is obtained by replacing i with j in the viscous flux form at $i+\frac{1}{2}$. This time the area used for Gauss integration to compute temrs u_x, u_y, etc. is shifted by $\frac{1}{2}$ in the η direction.

Using the above forms, the viscous flux terms are given finally as

$$\hat{F}_{v_{i+\frac{1}{2}}}-\hat{F}_{v_{i-\frac{1}{2}}}=\sum_{m=-2}^{2}\tilde{M}_{vm}q_{i+m}+\bar{\bar{F}}_{v_{i+\frac{1}{2}}}-\bar{\bar{F}}_{v_{i-\frac{1}{2}}} \tag{22}$$

$$\hat{G}_{v_{j+\frac{1}{2}}}-\hat{G}_{v_{j-\frac{1}{2}}}=\sum_{m=-2}^{2}\tilde{N}_{vm}q_{j+m}+\bar{\bar{G}}_{v_{j+1/2}}-\bar{\bar{G}}_{v_{j-\frac{1}{2}}} \tag{23}$$

where

$$\begin{cases}\tilde{M}_{v-2}=0\\ \tilde{M}_{v-1}=-\left[(kn_x)^{\epsilon}\frac{\partial F_v}{\partial q_-}+(kn_y)^{\epsilon}\frac{\partial G_v}{\partial q_-}\right]_{i-\frac{1}{2}}\\ \tilde{M}_{v0}=-\left[(kn_x)^{\epsilon}\frac{\partial F_v}{\partial q_+}+(kn_y)^{\epsilon}\frac{\partial G_v}{\partial q_+}\right]_{i-\frac{1}{2}}+\left[(kn_x)^{\epsilon}\frac{\partial F_v}{\partial q_-}+(kn_y)^{\epsilon}\frac{\partial G_v}{\partial q_-}\right]_{i+\frac{1}{2}}\end{cases}$$

$$\begin{cases}\tilde{M}_{v1}=\left[(kn_x)^{\xi}\dfrac{\partial F_v}{\partial q_+}+(kn_y)^{\xi}\dfrac{\partial G_v}{\partial q_+}\right]_{i+\frac{1}{2}}\\ \tilde{M}_{v2}=0\end{cases}$$

$$\bar{F}_{v_{i\pm\frac{1}{2}}}=[(kn_x)^{\xi}\bar{F}_v+(kn_y)^{\xi}\bar{G}_v]_{i\pm\frac{1}{2}}$$

and similarly with $\tilde{N}_v$ and $\hat{G}_v$. In the IAF procedure, $\hat{F}_v$ and $\hat{G}_v$ in the above equations are computed using the flow values at a previous timestep.

2.5 Approximate factorization

A Padé tjme differencing form is used for time integration. That is

$$\frac{\partial}{\partial t}=\frac{1}{\Delta t}\frac{\Delta}{1+\theta\Delta}\quad\text{where}\quad \Delta q^n=q^{n+1}-q^n \tag{24}$$

where the value θ is usually taken as 1, i.e. the Euler implicit. By substituting the flux forms of eqs.(16), (17), (22), and (23) into eq.(3), using the Padé time differencing, and applying the approximate factorization, finally results in

ξ-sweep

$$M_{-2}\Delta q^*_{i-2}+M_{-1}\Delta q^*_{i-1}+M_0\Delta q^*_i+M_1\Delta q^*_{i+1}+M_2\Delta q^*_{i+2}=RHS \tag{25}$$

where

$$M_m=\frac{\theta\Delta t}{S}(\tilde{M}+\tilde{M}_v)_m\quad(m=\pm1,\pm2)$$

$$=I+\frac{\theta\Delta t}{S}(\tilde{M}+\tilde{M}_v)_m\quad(m=0)$$

$$RHS=-\frac{\Delta t}{S}\Big[\sum_{m=-2}^{2}(\tilde{M}+\tilde{M}_v)_m q_{i+m}+\sum_{m=-2}^{2}(\tilde{N}+\tilde{N}_v)_m q_{j+m}+\hat{F}_{v_{i+1/2}}-\hat{F}_{v_{i-\frac{1}{2}}}+\hat{G}_{v_{j+1/2}}-\hat{G}_{v_{j-1/2}}\Big]^n-\frac{\theta\Delta t}{S}[\Delta\hat{F}_{v_{i+1/2}}-\Delta\hat{F}_{v_{i-1/2}}+\Delta\hat{G}_{v_{j+1/2}}-\Delta\hat{G}_{v_{j-1/2}}]^{n-1} \tag{26}$$

η-sweep

$$M_{-2}\Delta q^n_{j-2}+M_{-1}\Delta q^n_{j-1}+M_0\Delta q^n_j+M_1\Delta q^n_{j+1}+M_2\Delta q^n_{j+2}=\Delta q^*_j \tag{27}$$

where the metrics M_m are given similarly as in eq.(26).

Updating

$$q^{n+1}=q^n+\Delta q^n \tag{28}$$

2.6 Boundary conditions

Fig. 4(a) shows the topology of the O-grid used for computing flows past a circular cylinder, and Fig. 4(b) shows the corresponding map in the computational space.

At the left and right boundaries, the periodic boundary condition is used. At the bottom boundary, located at $j=1/2$, the solid wall boundary condition is used. For the inviscid flux $\hat{G}_{j-1/2}$ at $j=1$, an exact form is used instead of that given in eq.(14). Substituting $u=v=0$ and assuming that the pressure at $j=1/2$ is equal to that at $j=1$ (zero extrapolation by 1/2), it has the form as

$$\hat{G}_{j-\frac{1}{2}}=\begin{bmatrix}(kn_x)^{\eta}\\(kn_y)^{\eta}\\0\end{bmatrix}_{j-\frac{1}{2}}p_j\quad(j=1). \tag{29}$$

That is

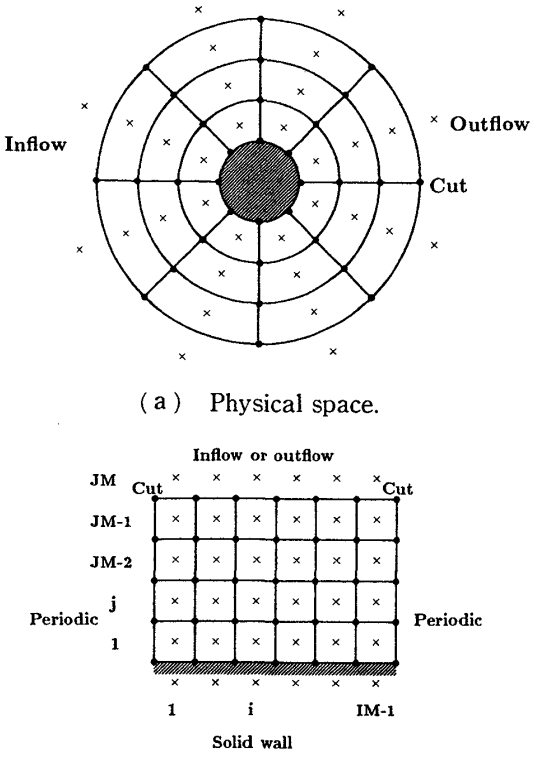

(a) Physical space.

(b) Computational space.

Fig. 4 Boundary conditions for circular cylinder.

$$\hat{G}_{j-\frac{1}{2}}=B_{wall}q_j\quad\text{where}\quad B_{wall}=\begin{bmatrix}0&0&(kn_x)^{\eta}\\0&0&(kn_y)^{\eta}\\0&0&0\end{bmatrix}_{j-\frac{1}{2}} \tag{29.a}$$

Th flux at $j+\frac{1}{2}$ is given in a simlilar manner as in eq. (14). This time the flux correction terms do not cancel out, and therefore must be taken into account. The viscous term $\hat{G}_{v_{j-1/2}}$ can be computed in the same manner as in the inner zone, if the value of q at $j=0$ is defined as

$$q_0=I_w q_1\quad\text{where}\quad I_w=\begin{bmatrix}-1&0&0\\0&-1&0\\0&0&1\end{bmatrix} \tag{30}$$

Then the velocities are computed as exactly zero at points on the wall, i.e. at the E and W points in Fig. 5.

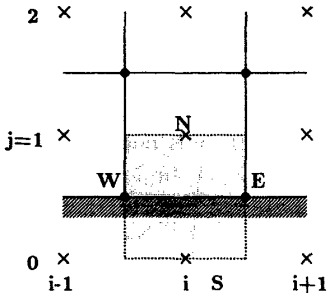

Fig. 5 Volume used for viscous term integration on solid wall.

At the outer boundary, two types of boundary conditions are used. One is the inflow boundary condition, and the other is the outflow boundary condition. The inflow condition is given as the uniform flow, i.e. $u=1$, $v=0$, and $p=0$. The outflow is given as the combination of zero extrapolation for u and v, and the given uniform flow value for p (i.e., $p=0$). In the both cases, a characteristic form of $\hat{G}_{j+1/2}$ is used as the boundary condition. That is, the flux form there is obtained by introducing an approximation of the characteristic nature to the exact form as shown below.

$$\begin{aligned}\hat{G}_{j+\frac{1}{2}}&=B^*_{j+\frac{1}{2}}q_{j+\frac{1}{2}} \qquad (j=JM-2)\\ &=(B^{*+}+B^{*-})_{j+\frac{1}{2}}q_{j+\frac{1}{2}}\\ &\doteqdot B^{*+}_{j+\frac{1}{2}}\left(\frac{3}{2}q_j-\frac{1}{2}q_{j-1}\right)+B^{*-}_{j+\frac{1}{2}}\left(\frac{3}{2}q_{j+1}-\frac{1}{2}q_{j+2}\right)\end{aligned} \tag{31}$$

where

$$B^{*\pm}_{j+\frac{1}{2}}=(R^*\Lambda^{*\pm}L^*)_{j+\frac{1}{2}} \tag{31.a}$$

where R^*, $A^{*\pm}$, and L^* are defined similarly as in eqs. (9), (10), (11).

The approximation in the last row of the eq.(31) is formally second-order accurate. The outer boundary is located at $j+1/2$ where $j=JM-2$ for coding conveniences. JM is the number of points in the j-direction. The terms in the outside region, i.e., q_{JM-1} and q_{JM} are referenced in the computation. They are given to be consistent with either inflow or outflow boundary condition. The Δq_{JM-1} and Δq_{JM} are given similarly.

In the governing equations corresponding to the control volumes adjacent to the top or bottom boundary, the $\tilde{N}$ terms need to be modified. That is

	$\Gamma^+_{-\frac{3}{2}}$	$\Gamma^+_{-\frac{1}{2}}$	$\Gamma^+_{\frac{1}{2}}$	$\Gamma^-_{-\frac{1}{2}}$	$\Gamma^-_{\frac{1}{2}}$	$\Gamma^-_{\frac{3}{2}}$
inner ($\xi-$, $\eta-$sweeps)	$-\Phi_1$	$1+\Phi_1-\Phi_2$	Φ_2	Φ_2	$1+\Phi_1-\Phi_2$	$-\Phi_1$
j = 1 ($\eta-$sweep)	0	Φ_1	Φ_2	0	$1-\Phi_2$	$-\Phi_1$
j = JM-2 ($\eta-$sweep)	$-\Phi_1$	$1-\Phi_2$	0	Φ_2	Φ_1	0

Further, terms related to flux-correction or wall boundary need to be added.

Fig. 6(a), (b) shows the grid topology used for a flat plate computation. The left edge of the flat plate is shifted by one grid cell to the right, in order to place the singularity point inside the flow. As the result, a gap appears at the bottom boundary in the computational space. The flux there exactly sums to zero. The velocity values at points edging the gap are needed to compute the viscous terms on the solid wall next to the gap. Their values can be computed by averaging as in normal points.

2.7 Global conservation

The forces acting on the body can be obtained by integrating the flux along the inner boundary.

$$[\text{Inner integration}]=F_{\text{bottom}}=-\sum_{i=1}^{IM-1}(\hat{G}_{j-\frac{1}{2}}+\hat{G}_{v_{j-1/2}})_{j=1} \tag{32}$$

The first component of F_{bottom} is equal to 1/2 of C_D, the drag coefficient. The second component is equal to 1/2 of C_L, the lift coefficient. The third component is the net

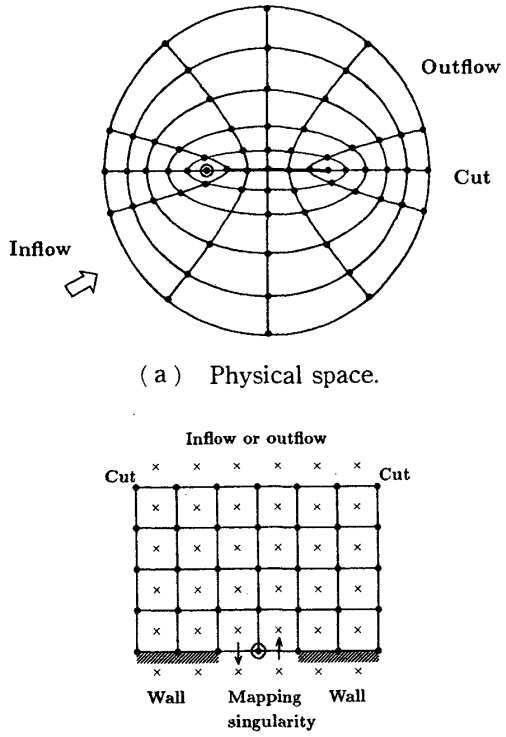

(a) Physical space.

(b) Computational space.

Fig. 6 Boundary conditions for a flat plate with mapping singularity.

mass flux, which is zero by definition. The forces can also be obtained by integrating, for example, at the outer boundary.

[Outer integration]

$$=F_{top}=-\sum_{i=1}^{IM-1}(\hat{G}_{j+\frac{1}{2}}+\hat{G}_{v_{j+1/2}})_{j=JM-2} \tag{33}$$

The integrated mass flux at the outer boundary should be zero at convergence. It is assured, by the form of the discretized governing equations, that the integrated inner and outer flux values agree with machine accuracy at convergence. That should also apply to the value obtained by adopting any control surface that surrounds the body and aligns piecewisely with the grid lines.

3. Computed Results

3.1 Circular cylinder

The flow past a circular cylinder of unit diameter was computed. The grid is shown in Fig. 7. The parameters used in the computation are

Reynolds number $R_e=40$.
Mimimum grid spacing $\Delta_{\min}=0.008$
Radius of outer boundary=40.0
Grid points in i-direction $IM=41$
Grid points in j-direction $JM=61$
$\theta=1.0$ (Euler implicit)
Pseudo-compressibility parameter $\beta=1.0$
Upwind differencing=3rd-order

The outflow boundary condition was imposed at

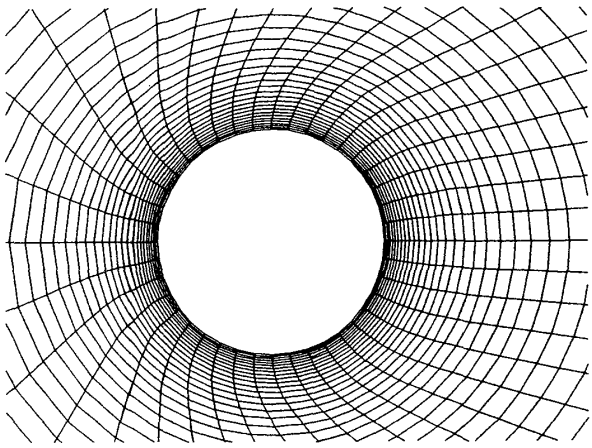

Fig. 7 Grid around a circular cylinder

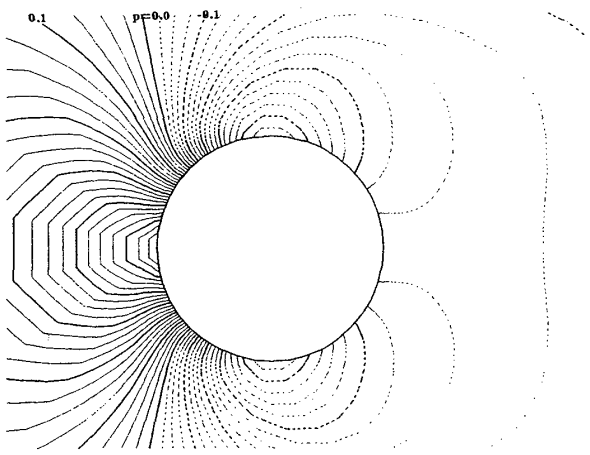

Fig. 8 Pressure contours.

points in the downstream zone that forms approximately 90 degrees angle at the center. At the time $t=0$, the flow was uniform everywhere. Computation was first made for 10 timesteps with $\Delta t=0.01$. Then Δt was changed to 1.0. In case $\beta=1.0$, the L2 norm of the residual Δq decreased to about 10^{-14} after 3000 timesteps. Fig. 8 shows pressure contours. The nondimensional pressure p is equal to 1/2 of the pressure coefficient C_p. Fig. 9 shows the surface pressure distribution. The angle θ is zero at the front stagnation point and 180 at the rear stagnation point. In the fine grid case, the number of grid is doubled both in ξ-and η-directions. It is seen that the difference is very small. Fornberg's computed result[16] shows slightly lower minimum pressure. The measured result by Grove[17] is still lower. The author suspects that the wall effect is non-negligible in Grove's result, in which the [wall distance/diameter] ratio is 20. Fig. 10 shows velocity vectors near a cylinder. The non-slip boundary condition is well satisfied.

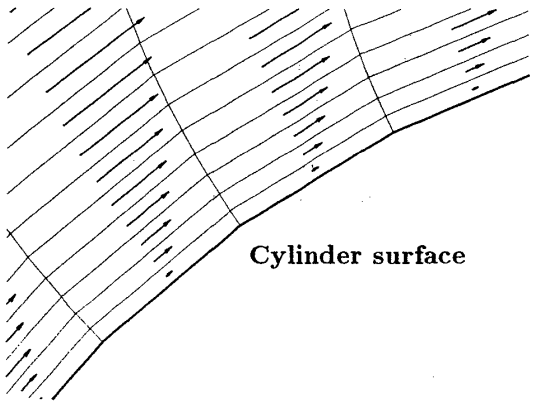

Fig. 10 Velocity vectors near a cylinder surface.

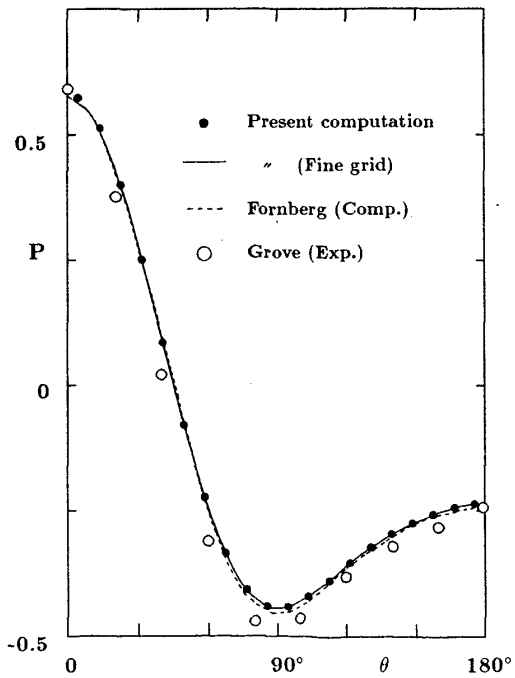

Fig. 9 Surface pressure distribution on a cylinder.

The integrated flux values are

$$F_{\text{bottom}}=\begin{bmatrix}0.75673968224135\\0.7218\times10^{-13}\\0\end{bmatrix},\quad F_{\text{top}}=\begin{bmatrix}0.75673968224303\\0.4807\times10^{-11}\\-0.3769\times10^{-11}\end{bmatrix}$$

where the components are, from top to bottom, drag, lift, and mass flow. It is evident that the global conservation holds with each component. The computed C_D values, which equal twice the nondimensional drag values, at $R_e=40$ are

Case	Present (β=1.0)	Present (β=4.0)	Fine grid (β=1.0)	Fornberg[16]	Dennis[18]
C_D	1.513	1.519	1.499	1.498	1.494

As pointed out in ref.[11], coupling occurs between the momentum equations and the continuity equation even in the steady-state limit, in the present upwind pseudo-compressibility approach. In order to check the degree of coupling, computations with $\beta=2.0$ and 4.0 were made. As shown in the above table, the obtained results did not show appreciable difference from the case $\beta=1.0$. In the fine grid case, the number of grid points were

doubled both in ξ-and η- directions. The fine grid value agrees well with other computed values. The measured C_D values[13] are

R_e	38.5	46.6	44.9	38.1	41.7
C_D	1.46	1.56	1.46	1.69	1.62

It is seen that the computed value is well within the scatter in the measured values.

The dependence of the computed results on the value of β was significantly increased by using zero extrapolation for pressure as well as velocities as the outflow boundary condition. That is the reason why the given uniform pressure value has been adopted as the outflow boundary condition. This suggests there is room for improvement in the outer boundary conditions. But clearly this dependence does not come from the coupling in the governing equations, and, as far as external flows are concerned, the present form of the boundary conditions is valid.

In order to check the influence of the grid topology, the same flow was computed using H-grid as shown in Fig. 11. Actual computation was made in the upper half zone with symmetry condition. The distances to upstream, downstream, and top boundaries are all 40. All the parameters used in the computation were the same as the O-grid case. Fig. 12 shows pressure contours. Though the distribution agrees well with the O-grid case, slight kinks are observed in the zones where the grid lines have kinks. The C_D value was 1.511, which differs by only 0.13 % from the O-grid value of 1.513.

3.2 Flat plate with mapping singularity

This case is to test the validity of the global conservation of the present scheme under the presence of mapping singularities. The parameters used are

Reynolds number $R_e=40$
Mimimum grid spacing $\Delta_{min}=0.008$
Radius of outer boundary=10.0
Grid points in i-direction $IM=21$
Grid points in j-direction $JM=21$
$\theta=1.0$ (Euler implicit)
Upwind differencing=3rd-order
Pseudo-compressibility $\beta=1.0$

Fig. 13 shows the grid used. The plate is flat with zero thickness. The inflow was set at 30 degrees to the flat plate. Except for the modifications needed to handle the gap, no modifications were made to the computer code used for the cylinder computations. The numerical stability limit was severer in this case, and Δt was limited to 0.05. The global conservation was again confirmed. Fig. 14 shows the velocity vectors, and Fig. 15 shows the pressure contours. At the points next to the leading edge, the pressure value becomes maximum on

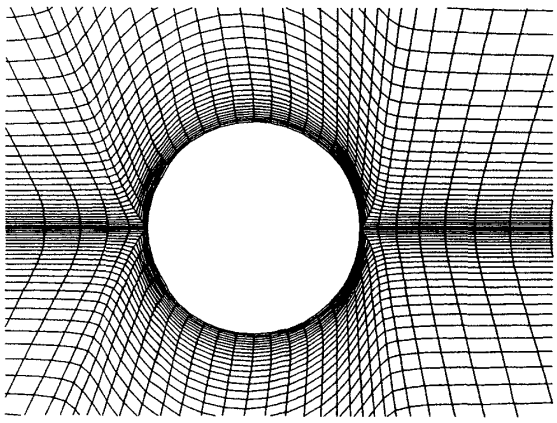

Fig. 11 Grid around a circular cylinder (H-grid).

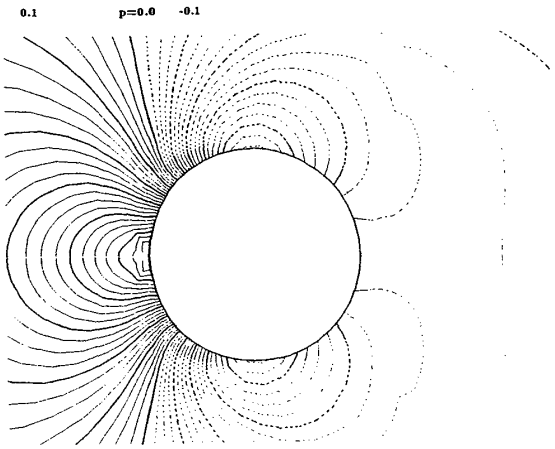

Fig. 12 Pressure contours (H-grid).

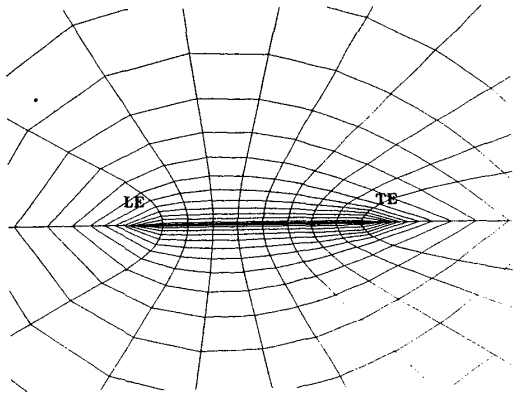

Fig. 13 Grid around a flat plate.

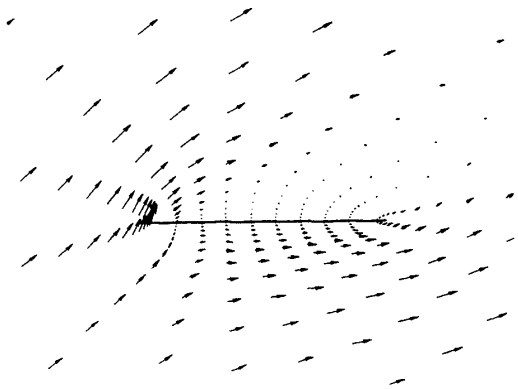

Fig. 14 Velocity vectors around a flat plate.

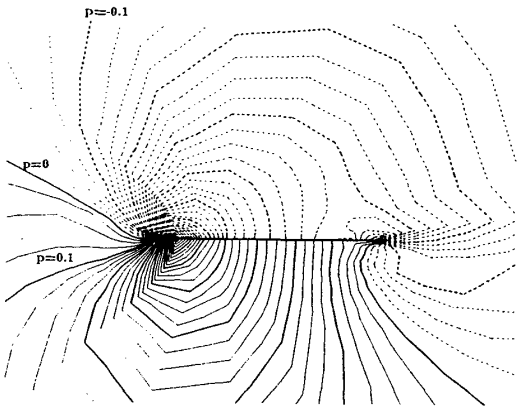

Fig. 15 Pressure contours around a flat plate.

the face side and minimum on the back side, and the velocity changes rapidly near the leading edge. In spite of this rapid change, oscillation is not observed in the pressure or velocity distribution. The global conservation was again confirmed, which demonstrates that the present scheme automatically circumvents the multi-valuedness or mapping singularity problem.

4. Conclusions

A finite-volume, cell-centered upwind scheme with pseudo-compressibility has been presented. It has the global conservation property, which means that the conservation property is satisfied all the way down to boundaries. With global conservation, the value of the forces acting on a body becomes independent of the integration path, whether along the body surface or along the outer boundary, and the computational scheme is made fully consistent with the way the forces are computed. It uses grid cells as control volumes, and facilitates the implementation of the global conservation property in a straightforward manner. Points of mapping singularity are automatically circumvented, and the global conservation property is not affected by the singularity points. The scheme is similar to the one[7] for compressible flows.

Computations were made for the flow past a circular cylinder at the Reynolds number R_e=40, using O-grid. The integrated flux values, i.e. lift, drag, and mass, agreed up to more than 11 significant figures after 1,000 timesteps, when they were integrated at the body and the outer boundary locations. The computed drag agreed well with other computed or measured results. The same flow was computed using H-grid. Though slight kinks appeared in the zones where kinks existed in the grid, the computed drag agreed well with the O-grid value, which seems to suggest that the global conservation property helps to make integrated force values independent of grids.

The flow past a flat plate with mapping singularity was computed at the Reynolds number R_e=40 and at the attack angle of 30 degrees. The global conservation property was not affected by the presence of the mapping singularity, though the numerical stability limit was severer in this case than in the circular cylinder case.

The present scheme has a room for improvement. It has a 3rd-order accuracy in the computational space, and not in the physical space. This causes the dependency on grids. Accuracy in the physical space should be pursued, taking into account the non-uniform spacing[19] or kinks[20] of grids. The degradation of numerical stability due to grid skewness is another problem. Further study is needed including the application of TVD limiters, related with it.

Acknowledgments

The author thanks the members of the CFD group at the Ship Research Institue for their valuable discussions.

References

[1] Yang, C. I., Hartwich, P. M., and Sumdaram, P. "Numerical Simulation of Three-Dimensional Viscous Flow around a Submersible Body", 5th International Conference on Numerical Ship Hydrodynamics (INC-5), Hiroshima, September 1989.

[2] Zhu, M., Miyata, H., and Kajitani, H. "Finite-Difference Simulation of a Viscous Flow about a Ship of Arbitrary Configuration", INC-5, Hiroshima, September 1989.

[3] Hino, T. "Computation of a Free Surface Flow around an Advancing Ship by the Navier-Stokes Equations", INC-5, Hiroshima, September 1989.

[4] Tzabiras, G. D. and Loukakis, T. A. "On the Numerical Solution of the Turbulent Flow-Field past Double Ship Hulls at Low and High Reynolds Numbers", INC-5, Hiroshima, September 1989.

[5] Kwag, S., Mori, K., and Shin, M. "Numerical Computation of 3-D Free Surface Flows by N-S Solver and Detection of Sub-breaking", J. of SNAJ vol. 166, (Dec. 1989).

[6] Kodama, Y. "Grid Generation and Flow Computation for Practical Ship Hull Forms and Propellers Using the Geometrical Method and the IAF Scheme", INC-5, Hiroshima, September 1989.

[7] Furukawa, M. et al. "A Zonal Approach for Solving the Compressible Navier-Stokes Equations Uning a TVD Finite Volume Method", Transactions of the Japan Society of Mechanical Engineers (B), Vol. 56, No. 523, March 1990.

[8] Chakravarthy, S., and Osher, S., "A New Class of High Accuracy TVD Schemes for Hyperbolic Conservation Laws", AIAA Paper 85-0363, 1985.

[9] Chakravarthy, S., et al, "Application of a New Class of High Accuracy TVD Schemes to the Navier-Stokes Equations", AIAA Paper 85-0165, 1985.

[10] Chakravarthy, S., "The Versatility and Reliability of Euler Solvers Based on High-Accuracy TVD Formulations", AIAA Paper 86-0243, 1986.

[11] Pan, D., and Chakravarthy, S., "Unified Formula-

tion for Incompressible Flows", AIAA Paper 89-0122, 1989.

[12] Roe, P. L., "Approximate Riemann Solvers, Parameter Vectors, and Difference Schemes", Journal of Computational Physics vol. 43, pp. 357-372, 1981.

[13] Tritton, D. J., "Experiments on the Flow Past a Circular Cylinder at Low Reynolds Numbers", Journal of Fluid Mechanics vol. 6, pp. 547-567, 1959.

[14] Ferziger, J. H., "Numerical Methods for Engineering Application", John Wiley & Sons, 1981.

[15] Kodama, Y., "Computation of the Two-Dimensional Incompressible Navier-Stokes Equations for Flow Past a Circular Cylinder Using an Implicit Factored Method", Papers of Ship Research Institute vol. 22, No. 4, 1985.

[16] Fornberg, B., "A Numerical Study of Steady Viscous Flow Past a Circular Cylinder", J. F. M., vol. 98, part 4, pp. 819-855, 1980.

[17] Grove, A. S. et al., "An Experimental Investigation of the Steady Separated Flow Past a Circular Cylinder", J. F. M., vol. 19, part 1, pp. 60-80, 1964.

[18] Dennis, S. C. R., "A Numerical Method for Calculating Steady Flow Past a Cylinder", Proceedings of 5th International Conference on Numerical Methods in Fluid Dynamics, Lecture Notes in Physics 59, pp. 165-172, 1976.

[19] Sawada, K. and Takanashi, S., "A Numerical Investigation on Wing/Nacelle Interferences of USB Configuration", AIAA Paper 87-0455, 1987.

[20] Sawada, K. and Takanashi, S., "On the Accuracy of Upwind Biased Finite Volume Method", 5th NAL Symposium on Aircraft Computational Aerodynamics, National Aerospace Laboratory, 1987.